

# Studying topological structure in the epoch of reionization with 3D-Minkowski functionals of 21cm line fluctuations

Shintaro Yoshiura<sup>1</sup>\*, Hayato Shimabukuro<sup>1,2</sup>, Keitaro Takahashi<sup>1</sup>, and Takahiko Matsubara<sup>2</sup>

<sup>1</sup>*Department of Physics, Kumamoto University, Kumamoto, Japan*

<sup>2</sup>*Department of Physics, Nagoya University, Aichi, Japan*

Accepted XXX. Received YYY; in original form ZZZ

## ABSTRACT

The brightness temperature of redshifted 21cm line brings rich information on the IGM (Inter Galactic Medium) through the Dark Ages to the Epoch of Reionization (EoR). While the power spectrum is a useful tool to statistically investigate the 21cm signal, it is not sufficient to fully understand the 21cm brightness temperature field because it is expected to be highly non-gaussian distribution. Minkowski Functionals (MFs) are a promising tool to extract non-gaussian feature of the 21cm signal and will give topological information such as morphology of ionized bubbles. The ionized bubbles make typical image on the map but the brightness temperature also consists of the matter density and the spin temperature fluctuations. In this work, we study the 21cm line signal in detail with MFs. To promote understanding of basic features of the 21cm signal, we calculate the MFs of the components which contribute to the brightness temperature fluctuations. We find that the structure of the brightness temperature mainly depends on the ionized fraction on spin temperature. The general property which is independent of bubble shape is also found out by using different reionization models. In addition, the MFs are sensitive to the parameter which is related to topology of ionized bubbles and we consider the possibility of constraining parameters with the MFs of future 21cm-line signal observations.

**Key words:** methods: statistical—cosmology: dark ages, reionization, first stars—large-scale structure of Universe

## 1 INTRODUCTION

After the cosmic recombination, hydrogen keeps neutral state until first luminous objects such as stars and galaxies are formed. As structure formation advances, neutral hydrogen begins to be ionized by the UV photons escaped from galaxies. This epoch is called “Epoch of Reionization”. Many theoretical works based on both numerical simulations and analytic models have investigated the time evolution and spatial structure of ionized bubbles in the EoR (Mesinger et al. 2011; McQuinn et al. 2007; Zahn et al. 2007). We can subtract the information on the state of the IGM in the EoR through the redshifted 21cm line due to the hyperfine structure of neutral hydrogen (Furlanetto et al. 2006).

However, the 21cm signal from the EoR has not been accessible yet. Ongoing interferometers such as Murchison Widefield Array (MWA) (Lonsdale et al. 2009; Tingay et al.

2013; Beardsley et al. 2013), LOw Frequency ARray (LOFAR) (van Haarlem et al. 2013; Jensen et al. 2013), and Precision Array for Probing the Epoch of Reionization (PAPER) (Parsons et al. 2010, 2014) have already started observation to detect 21cm signal statistically. In fact, the MWA and the PAPER have already obtained upper limits on the 21cm power spectrum (Dillon et al. 2015). The Square Kilometer Array (SKA), a future project of low-frequency radio interferometer, will start observation in the near future (Carilli 2015) and it has a large field-of-view, high sensitivity and high angular resolution necessary for imaging of the 21cm-line signal.

In order to understand the thermal and ionization state of the IGM, the power spectrum has often been used for statistical analyses of the fluctuations in the 21cm brightness temperature field. For example, the typical bubble size can be known through the “shoulder” of the 21cm power spectrum (Pritchard & Furlanetto 2007; Pober et al. 2014; Shimabukuro et al. 2014; Furlanetto et al. 2006; Mesinger et al. 2014). Although the power spectrum is a

\* E-mail: 147d8012@st.kumamoto-u.ac.jp

powerful tool, it is not perfect to describe the statistical property of the 21cm-signal fluctuations because they follow a highly non-gaussian probability distribution due to complicated ionizing processes. Therefore, higher order statistics such as the bispectrum (Shimabukuro et al. 2015) and trispectrum (Cooray et al. 2008) are required to evaluate non-gaussianity.

As reionization process advances, many ionized bubbles appear and these bubbles have typical topological structures in the brightness temperature field. The Minkowski Functionals (MFs) are useful tools to characterize these topology. In the context of observational cosmology, the MFs have been used to investigate the geometrical feature of galaxy distribution (Gott et al. 1986; Schmalzing & Buchert 1997) and to estimate non-gaussianity appeared in the CMB temperature map (Komatsu et al. 2009). In this study, we apply the MFs to three dimensional brightness temperature field. Other works also studied the topological property of the brightness temperature field (Gleser et al. 2006; Lee et al. 2008; Friedrich et al. 2011; Hong et al. 2014).

The MFs and genus have been used to characterize the topology of HI distribution in the EoR. The topology varies with the evolution of ionization and the different stages of reionization could be distinguished by the MFs and genus (Lee et al. 2008). The topological property was utilized for suggesting a semi-numerical model which reproduces the MFs obtained from simulation with radiative transfer of ionizing photon (Gleser et al. 2006), and for investigating dependency of HI topology on ionizing source property (Friedrich et al. 2011). In addition, the distribution of the 21cm line brightness temperature has been studied by the 2D genus (Hong et al. 2014; Wang et al. 2015). Then, the  $\delta T_b$  have been assumed  $T_S \gg T_\gamma$  which is a suitable condition at the epoch where the spin temperature is sufficiently larger than the CMB temperature. They have found that genus curves depend on the ionized fraction, discriminate the scenarios with different ionizing efficiency.

Previous works mainly apply the MFs to both HI distribution and brightness temperature maps with an assumption that the spin-temperature fluctuations do not contribute to those in the brightness temperature since the mean spin temperature is expected to be much larger than the CMB temperature as the result of X-ray heating. Although this assumption is frequently used, it depends on the property of X-ray sources. On the other hand, we apply the MFs to brightness temperature fields including the effects of spin temperature and compare EoR models.

In this paper, we calculate the 3-dimensional MFs of the 21cm brightness temperature. The brightness temperature fluctuations consist of three components: fluctuations in neutral fraction, spin temperature and matter density. Firstly, we study the MFs of these components and obtain an insight into those of the brightness temperature. Secondly, in order to study the general property of the MFs which is independent of reionization models, we investigate the redshift evolution of the MFs and compare it between different ionization models. Finally, to study the dependence of MFs on ionized bubble property such as size, shape and distribution, we calculate the MFs varying key model parameters.

This paper is organized as follows. In section 2, we explain the brightness temperature, semi-numerical simulation

21cmFAST and our models. In section 3 we introduce the Minkowski Functionals. Our main results about a comparison of the MFs between different models are presented in section 4. The summary and discussion will be given in section 5. Throughout this paper, we assume  $\Lambda$ CDM cosmology with  $(\Omega_m, \Omega_\Lambda, \Omega_b, H_0) = (0.27, 0.73, 0.046, 70 \text{km/s/Mpc})$  (Komatsu et al. 2011).

## 2 SET UP : SIMULATION MODEL

The observable for the 21cm line is the brightness temperature defined by the difference between the spin temperature and the CMB temperature (Mesinger et al. 2011; Furlanetto et al. 2006). The 3D mapped the brightness temperature has rich information on thermal and ionized state at the EoR. The brightness temperature is defined by

$$\delta T_b(z) \approx 27x_{\text{HI}}(1 + \delta_m) \left( \frac{H}{dv_r/dr + H} \right) \left( 1 - \frac{T_\gamma}{T_S} \right) \times \left( \frac{1+z}{10} \frac{0.15}{\Omega_m h^2} \right)^{1/2} \left( \frac{\Omega_b h^2}{0.023} \right) [\text{mK}], \quad (1)$$

where  $H$  is the Hubble parameter,  $dv_r/dr$  is the peculiar velocity,  $\Omega_m$  is the matter density parameter,  $\Omega_b$  is the baryon density parameter and  $h$  is the Hubble constant,  $x_{\text{HI}}$  is the neutral fraction,  $\delta_m$  is the density contrast of matter,  $T_S$  is the spin temperature and  $T_\gamma$  is the CMB temperature. The spin temperature couples to kinetic temperature of IGM through the Wouthuysen-Field (WF) effect (Pritchard & Furlanetto 2006) and reflects the thermal state of IGM. When the IGM is heated sufficiently by X-ray photons emitted from bright sources, the spin temperature is much larger than the CMB temperature and the factor  $(1 - T_\gamma/T_S)$  is saturated. Therefore, the  $T_S$  is usually ignored when the spin temperature is much larger than the CMB temperature, especially at the EoR. The fluctuation of  $\delta T_b$  is expressed by

$$\delta_{21}(\mathbf{x}, z) = \frac{\delta T_b(\mathbf{x}, z) - \overline{\delta T_b}(z)}{\overline{\delta T_b}(z)}. \quad (2)$$

Here,  $\overline{\delta T_b}$  is spacial average value of the brightness temperature in the volume.

We make brightness temperature maps by using a semi-numerical simulation code 21cmFAST (Mesinger et al. 2011). In order to calculate  $\delta T_b$ , we use three maps such as neutral fraction  $x_{\text{HI}}$ , matter density  $\delta_m$  and spin temperature  $T_S$  obtained from 21cmFAST at various redshifts. In 21cmFAST, the matter density is calculated by using the Zel'dovich approximation and this code calculates spin temperature by taking into account X-ray heating and the intensity of Lyman alpha emission based on analytic model. The ionized fraction is also calculated by analytic model developed by (Furlanetto et al. 2004). We recommend readers to see (Mesinger et al. 2011) for more detail of calculation.

We refer standard model as “fid”. In this model  $\delta T_b$  is calculated by Eq. (1). To compare “fid” with each of component distribution, we prepare three kinds of maps. The component map “ $T_S$ ” uses only the spin temperature map to calculate  $\delta T_b$ , ignoring the fluctuation of  $x_{\text{HI}}$  and  $\delta_m$  (i.e.  $x_{\text{HI}}(\mathbf{x}, z) = \overline{x_{\text{HI}}}(z)$  and  $\delta_m(\mathbf{x}) = 0$ ). The component map “ $m$ ” considers only the matter density fluctuations and ignores

the fluctuations in  $x_{\text{HI}}$  with an assumption  $T_S \gg T_\gamma$ . The component map “ $x_{\text{H}}$ ” uses only the fluctuation of neutral hydrogen fraction with  $\delta_m = 0$  and  $T_S \gg T_\gamma$ . The MFs calculated from these maps represent the structure of components because their fluctuation is determined only by a single component. In section 4.1, we compare the MFs of these maps with one of “fid”.

We prepare another model to evaluate effect of the bubble property on MFs. In 21cmFAST, ionized bubbles are produced by analytic model based on prescription developed by [Furlanetto et al. \(2004\)](#). In order to study the effect of bubble shape on topology of bubbles, bubbles have a spherical shape in this model. The 21cmFAST provides us matter density fields at various redshifts. We use a matter density field at  $z = 8.58$ , which variance is  $\sigma_m^2 = 0.24$ , to make fields of this “spherical bubble” model (here after SB-model). The distribution of ionizing sources in this model is in common with our fiducial model since these models have same matter density field. We make spherical bubbles with radius  $R_b$  around cells if  $\delta_m(\mathbf{x})$  becomes larger than threshold value  $\delta_{\text{th}}^{\text{SB}}$ . We assumed that hydrogen is fully ionized ( $x_{\text{HI}} = 0$ ) in the bubbles and completely neutral ( $x_{\text{HI}} = 1$ ) outside the bubbles. Because we use the assumption  $T_S \gg T_\gamma$ , the brightness temperature can be described as  $\delta T_b(x) \propto x_{\text{HI}}(1 + \delta_m(x))$ . We parametrize the radius of bubbles  $R_b$  and  $\delta_{\text{th}}^{\text{SB}}$  in SB-model. These parameters,  $R_b$  and  $\delta_{\text{th}}^{\text{SB}}$ , are related to  $\zeta_{\text{ion}}$  and  $T_{\text{vir}}^{\text{min}}$  respectively. The difference between SB-model and “fid” is the property of ionized bubbles such as their size and shape. In order to get physical interpretation about various of the MFs that we compare SB model with “fid”.

We compare models which have different parameters with the “fid” model. Here we focus on two parameters. One of them is the ionizing efficiency  $\zeta$  which is a product of the fraction of gas converted into stars, the escape fraction and number of ionizing photon produced per solar baryon ([Mesinger et al. 2014](#)). The other parameter we focus on is the minimum virial temperature,  $T_{\text{vir}}^{\text{min}}$ . This parameter controls the minimum mass of ionizing sources. The “fid” model has  $\zeta = 15$ ,  $T_{\text{vir}}^{\text{min}} = 10^4$ [K] whose values are set in order to finish reionization at  $z = 6$  which recommended from observation of high- $z$  quasar spectra ([Fan et al. 2006](#)). We study the effect of the minimum virial temperature,  $T_{\text{vir}}^{\text{min}}$ , on topology of bubbles. The virial temperature is important for topology of the EoR. The reason is following one. Even low mass halos can be ionizing sources when we set  $T_{\text{vir}}^{\text{min}}$  small. The bubble size is proportional to the mass of sources, and therefore, a large number of ionizing sources make many small ionized bubbles. On the other hand, some large ionized bubbles are made by the ionizing source in the high mass halo in the case that  $T_{\text{vir}}^{\text{min}}$  is large ([Kim et al. 2013](#)). We often use  $T_{\text{vir}}^{\text{min}} = 1 \times 10^4$ [K], which value is criterion that atomic cooling becomes effective. Below this value, atomic cooling is ineffective and molecular cooling due to the oscillation and rotation of molecular hydrogen becomes main effective in stead of atomic cooling. However, if there are radiative feedback processes such as photodissociation, star formation in halo is suppressed because the molecular hydrogen is destroyed and the molecular cooling also becomes ineffective ([Haiman et al. 2000](#); [Hasegawa & Semelin 2013](#)).

### 3 MINKOWSKI FUNCTIONALS

MFs are a useful tool to investigate the topological structure of distribution. We can subtract topological information on arbitrary scalar function  $p(\mathbf{x})$  distributed in 3D space via the MFs. The excursion set  $F_\nu$  consists of all  $p(\mathbf{x})$  which satisfy  $p(\mathbf{x}) > p_{\text{th}}$ . Here,  $p_{\text{th}}$  is threshold value defined as  $p_{\text{th}} = \nu\sigma$  and  $\sigma^2(\langle p^2(\mathbf{x}) \rangle)$  is a variance of  $p(\mathbf{x})$  which average is zero in volume  $V$ . We can set  $\nu$  arbitrary. The definitions of MFs are given by ([Gleser et al. 2006](#)) as a function of  $\nu$

$$V_0(\nu) = \frac{1}{V} \int_V d^3x \Theta(p(\mathbf{x}) - \nu\sigma), \quad (3)$$

$$V_1(\nu) = \frac{1}{6V} \int_{\partial F_\nu} ds, \quad (4)$$

$$V_2(\nu) = \frac{1}{6\pi V} \int_{\partial F_\nu} ds [\kappa_1(\mathbf{x}) + \kappa_2(\mathbf{x})], \quad (5)$$

$$V_3(\nu) = \frac{1}{4\pi V} \int_{\partial F_\nu} ds \kappa_1(\mathbf{x}) \kappa_2(\mathbf{x}), \quad (6)$$

where  $\Theta$  is the Heaviside step function,  $\partial F_\nu$  is the surface of excursion set and  $ds$  is surface element.  $\kappa_1$  and  $\kappa_2$  are curvatures on the surface. The  $V_0$  shows the volume of excursion set. Total surface and mean curvature of  $F_\nu$  correspond to  $V_1$  and  $V_2$  respectively. The  $V_3$  is the Euler characteristic which describes typical shape of  $F_\nu$ . The Euler characteristic  $\chi$  is related to genus  $g$  as  $\chi = 2(1 - g)$ . For instance, a sphere has  $\chi = 2$  ( $g = 0$ ) and a torus has  $\chi = 0$  ( $g = 1$ ). If the  $V_3$  has positive value, there are many isolated excursion sets. Negative value of  $V_3$ , on the other hand, means that the excursion set has a multi-connected structure. The calculation method of the MFs is shown in [Gleser et al. \(2006\)](#) and [Schmalzing & Buchert \(1997\)](#).

If  $p(x)$  has gaussian distribution, the MFs can be written analytically and have symmetric shape. We show the MFs for gaussian distribution in Fig. 1. For example, the  $V_3$  has two positive peaks at higher and lower  $\nu$  and has a negative peak at center of  $\nu$  which corresponds to average value of  $p(x)$ . These two peaks reflect symmetric probability distribution function of gaussian distribution which means that there are same number of isolated regions which have positive and negative value. For non-gaussian distribution, this symmetry is broken. When the non-gaussianity is weak, the MFs can be described analytically ([Matsubara 1994](#)). As we will see below, the MFs of  $\delta T_b$  are absolutely different from one of gaussian case because  $\delta T_b$  has highly non-gaussian distribution.

We use  $p(x)$  smoothed by gaussian kernel which is expressed by  $\exp(-k^2 R^2/2)$  in Fourier space. Here,  $k$  is a wave number and  $R$  is smoothing scale. Throughout this paper, we set  $R=5$ Mpc. We find that the smoothing scales changes the shapes of MFs, but the shapes of MFs does not depend on  $R$  so much for  $R>5$ Mpc. Here, we refer the spacial resolution of the SKA1-low aimed at observing the 21cm signals. The spacial resolution at  $z \sim 10$  is  $\sim 5$  Mpc for the SKA1-low. This is why we choice  $R=5$  Mpc as our fiducial smoothing scales. Note that ionized bubbles which radius is smaller than smoothing scale  $R$  is erased by performing smoothing. Therefore, although the brightness temperature at ionized regions should become zero, this does not become precisely zero if we perform smoothing with large smoothing scale  $R$ . We call this region “unresolved ionized” region.

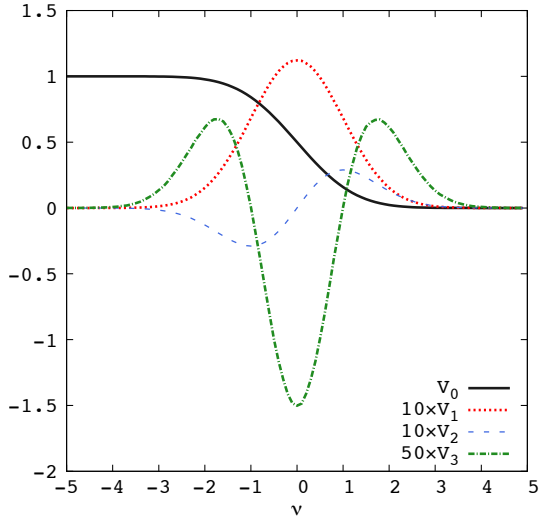


Figure 1. The Minkowski functionals for gaussian distribution.

## 4 RESULTS

The 21cm brightness temperature is expected to have a non-gaussian distribution due to the highly-nonlinear astrophysical effects. The MFs are one of the useful methods to evaluate complicated topological structure of 3D distribution even if it has non-gaussian shape. However, it is not straightforward to put a physical interpretation from the MFs. Therefore, in this section to promote understanding the MFs, we compare different EoR models and try to comprehend topological features of the brightness temperature distribution.

### 4.1 The Components of brightness temperature

Since the brightness temperature consists of the spin temperature, neutral hydrogen fraction and matter density fluctuation, it has rich information on both the cosmology and astrophysics. Topology of the brightness temperature in the EoR is expected to reflect all these components. In particular, ionized bubbles imprint unique topology on  $\delta T_b$  map. Furthermore, the spin temperature is also one of the important components of  $\delta T_b$ . However, the effect of spin temperature can be ignored at the epoch when kinetic temperature is sufficiently heated much more than the CMB temperature ( $T_s \gg T_\gamma$ ). In this subsection, we compare  $V_3$  of “fid” with the one of “ $T_s$ ”, “m” and “ $x_H$ ” to study which component is effective for the structure of  $\delta T_b$ .

In Fig. 2, we show the brightness temperature maps for three components at  $z=8.58$ . The average value of the spin temperature is  $581.1[K]$  which is much larger than the CMB temperature  $T_\gamma = 26.12[K]$ . In this case, fluctuations of the spin temperature does not contribute to  $\delta T_b$  because the IGM is heated sufficiently at  $z = 8.56$ . Therefore, the map of “ $T_s$ ” looks smoothed evenly. The map of model “m” has hot (cold) regions corresponding to high (low) density region. Because there are ionized sources in these high dense regions, ionized bubbles are located at around these regions as can be seen in the middle panel of Fig. 2.

The Fig. 3 shows  $V_3$  of four models “fid”, “ $T_s$ ”, “m” and “ $x_H$ ” at redshift  $z=7.50, 8.58, 11.90$  and  $15.13$  with smoothing scale  $5 \text{ Mpc}$ . In Fig. 4, we show maps of  $\delta T_b$  of model

“fid” at each redshifts for reference. We discuss both the behavior of the MFs for “fid” model and the relation between “fid” and component maps.

At  $z=7.50$ , as one can see in the top left panel of Fig. 3, the  $V_3$  of “m” has two positive peaks and one negative peak similar to in the case of gaussian distribution. It has the break of symmetry caused from nonlinearity of gravity. However, “ $x_H$ ” and “fid” lose a positive peak at lower  $\nu$ . As we can see in top left panel of Fig. 3, the  $V_3$  of “fid” and “ $x_H$ ” have the same shape except their amplitudes. This suggests that the distribution of  $\delta T_b$  is determined by the distribution of ionized fraction and matter density has no effect on the structure of IGM. The  $\delta T_b$  is small at higher dense region because of ionizing sources in the region. Therefore, we can understand  $V_3$  as below. The positive peak at lower  $\nu$  represents the abundance of isolated lower dense region for “m” and the peak corresponds to ionized region for “ $x_H$ ”. After ionized bubbles are merged, however, these bubbles make a connected region which has handles of isolated neutral regions at  $z = 7.50$ . This connected region corresponds to negative  $V_3$ .

The  $V_3$  of “fid” at  $z=8.58$  has similar property to one at  $z=7.50$ . It has a small positive peak at  $\nu=-2$ . The peak represents that there are isolated regions, in which  $\delta T_b$  is small. It is indicated that, as we can see in middle panel of Fig. 2, ionized bubbles are not as large as it merges each other.

At  $z=11.90$ , the spin temperature  $T_s = 99[K]$  is not much larger than  $T_\gamma = 36[K]$  and neutral hydrogen begins to be ionized at high dense regions. The shape of  $V_3$  does not trace any components in bottom left panel of Fig. 3. Therefore, it is expected that all components (the matter density fluctuation, neutral fraction and spin temperature) contribute to the structure of the brightness temperature and they make  $\delta T_b$  complicated.

We note that the meaning of  $\nu$  changes to be opposite at  $z=15.13$  because the average brightness temperature is negative and then high  $\delta T_b$  corresponds to negative value of  $\delta$  as it is defied by eq.2. That is, the peak of at positive  $\nu$  shows that there are many isolated cooler regions and one at negative means that hotter regions. The  $V_3$  of “ $T_s$ ” has two positive peaks. The left peak is higher than others differently from gaussian case. This represents many isolated region heated by X-ray photons. At this redshift, X-ray photons are emitted by sources and begin to heat the IGM gas around the sources. This leads to make isolated heated regions around sources. As you can see in bottom right panel of Fig. 3, although  $V_3$  of “fid” are completely different from “m” and “ $x_H$ ”, “ $T_s$ ” have similar feature. This indicates that the main component of  $\delta T_b$  is spin temperature at early stage of the EoR in this model. At these redshifts, almost all of hydrogen are neutral and this makes  $\delta T_b$  not to depend on  $x_{HI}$ . Therefore, “fid” and “ $T_s$ ” have same shape.

Generally, the spin temperature can be ignored at low redshift. However, the  $V_3$  at  $z=11.90$  and  $15.13$  has asymmetry for shape caused by the spin temperature. Because the spin temperature is obviously lower than the CMB temperature at  $z=15.13$  in our model, the average value of the brightness temperature becomes negative. For such situation, we should not use the assumption that the spin temperature is much larger than the CMB temperature. However, at  $z=11.90$  the average value of the  $\delta T_b$  is positive and it is

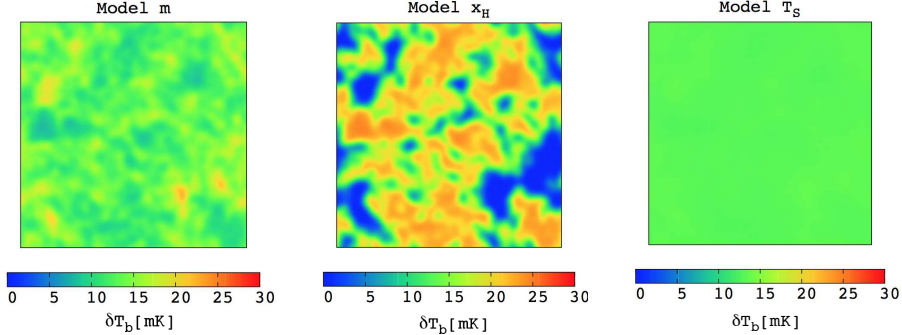


**Figure 2.** Maps of the brightness temperature for three components. The panels are corresponding to map “m”, “ $x_H$ ” and “ $T_S$ ” from left to right. We show name of maps above each panels. The redshifts is 8.58 for all of them.

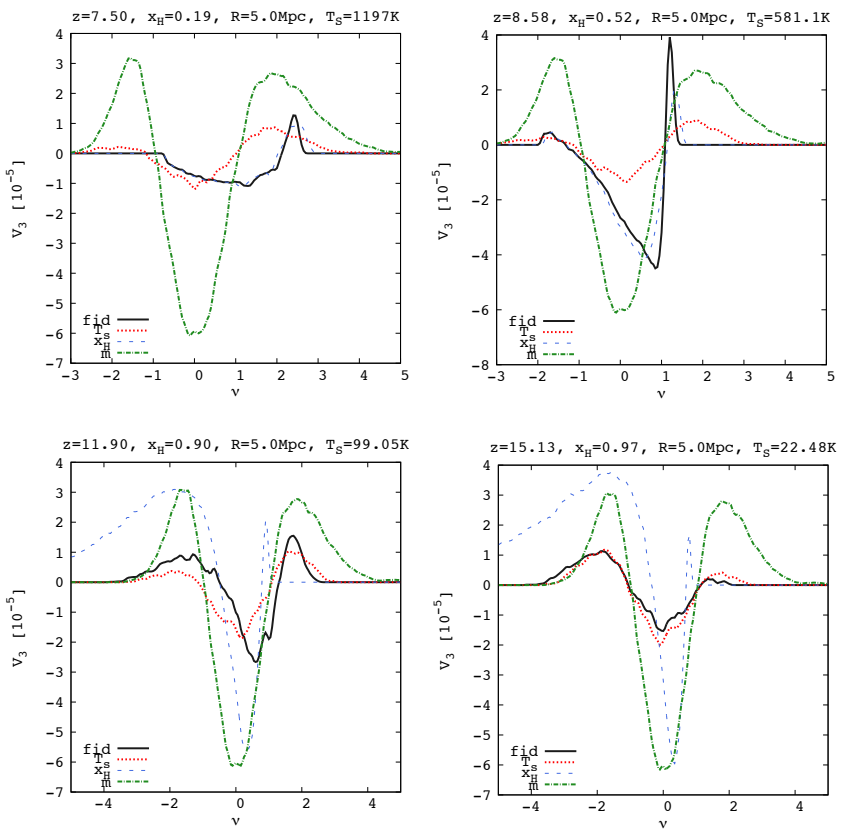


**Figure 3.** Comparing about components. The smoothing scales is  $R=5\text{Mpc}$ . The redshifts are 7.50, 8.58, 11.90 and 15.13 from top to bottom. We compare model “fid” (solid line), “ $T_S$ ” (dotted line), “ $x_H$ ”(dashed line) and “m” (dot dashed line).

not evident whether spin temperature affects the structure of  $\delta T_b$  or not. Consequently, we have to be careful to use the assumption referred above.

## 4.2 Redshift evolution of MFs

Here, we focus on the redshift evolution of MFs. The Fig. 5 shows the MFs as a function of  $\delta T_b$ , instead of  $\nu$ , at four kind of redshift (7.50, 8.02, 8.58, 9.95).

As ionized bubbles in which  $\delta T_b = 0 \text{ mK}$  become large, volume of neutral region in which  $\delta T_b(x) > 0 \text{ mK}$  decreases. Therefore, as we can see the top left panel of Fig. 5, the  $V_0$  also decreases at  $\delta T_b > 0 \text{ [mK]}$ . However, these decreased

values do not correspond to the volume ionized fraction (e.g.  $x_{HI} = 0.52$  at  $z=8.58$ ). The reason is that some ionized regions are smoothed and these regions have non-zero  $\delta T_b$ . The  $V_0$  of gaussian distribution does not decrease sharply, as we can see in Fig. 1. This decrease is a typical shape of  $V_0$  of  $\delta T_b$  and it becomes conspicuous at lower  $z$ .

The  $V_1$  represents area of excursion set. In the case of gaussian distribution, the  $V_1$  has a symmetric peak. However, as we can see in top right panel of Fig. 5, the peak is not symmetric and the peak shifts from right to left. This result reflects both contraction of neutral regions and expansion of ionized regions. In bottom left panel of Fig. 5, negative peaks of the  $V_2$  also shift from right to left. Al-

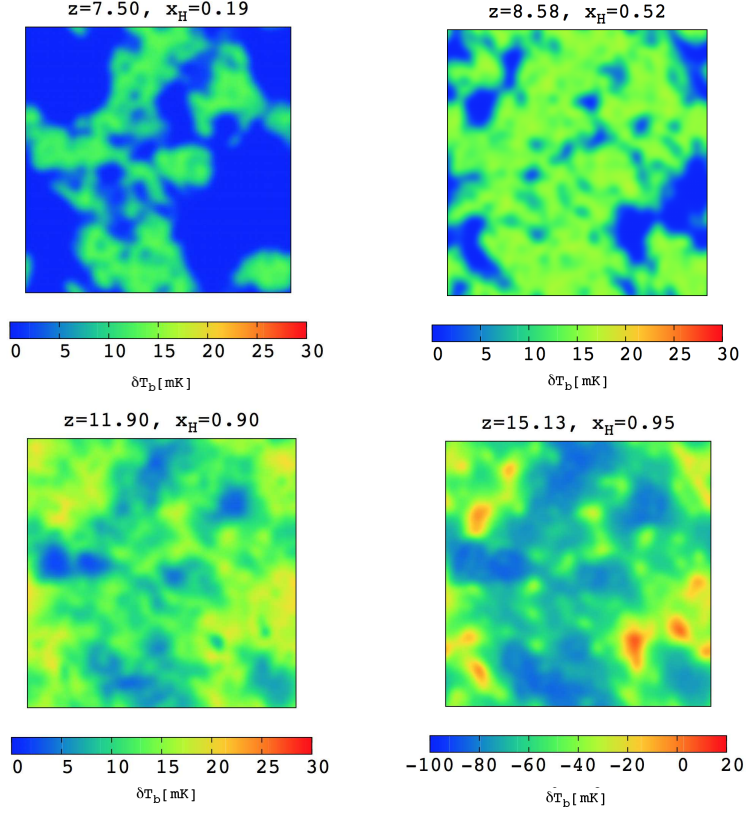


**Figure 4.** Maps of the brightness temperature for model “fid”. The panels are corresponding to redshift  $z=7.50, 8.58, 11.90$  and  $15.13$ . We show neutral fraction  $x_{\text{HI}}$  and average brightness temperature above each panels.

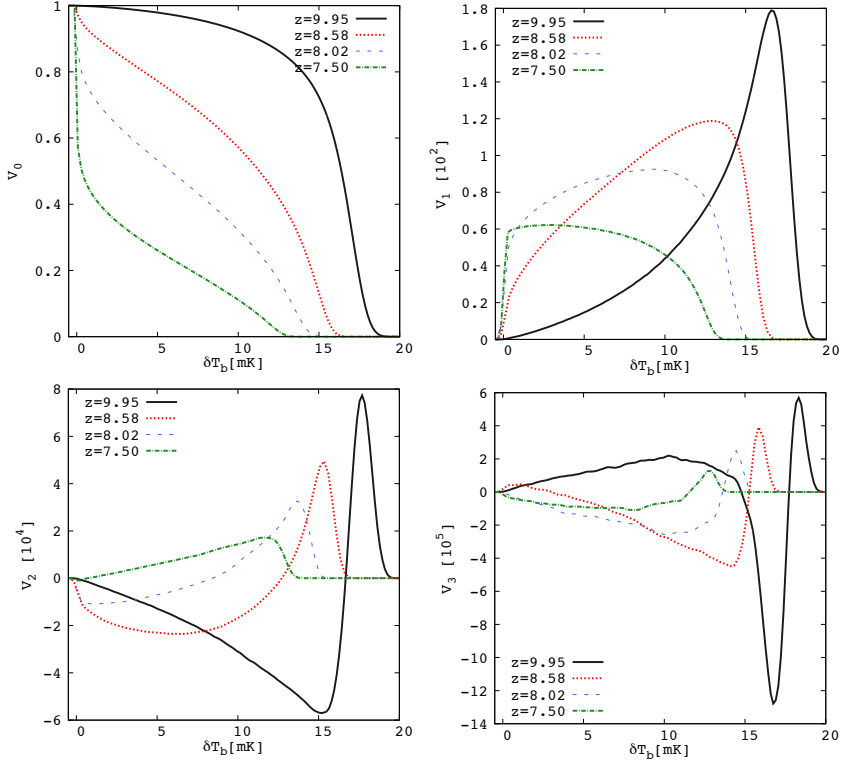


**Figure 5.** MFs of model “fid” brightness temperature at  $z = 7.50, 8.02, 8.58$  and  $9.95$ .

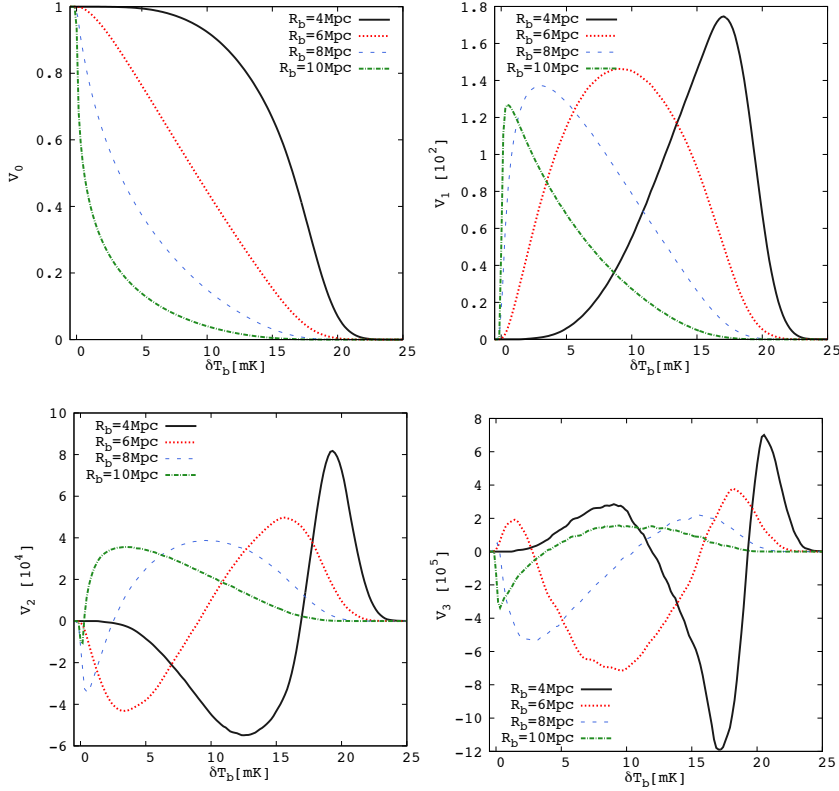


Figure 6. MFs of SB-model brightness temperature. The threshold value  $\delta_{\text{th}}^{\text{SB}} = 4\sigma_m$

though the  $V_2$  of gaussian distribution has point symmetric shape, at lower redshifts except  $z=7.50$ ,  $V_2$  has a negative wide peak and a positive sharp peak. On the other hand, the  $V_2$  has only positive value at  $z = 7.50$ .

The  $V_3$  represents the topological information. Generally, the  $V_3$  has two positive peaks at high and low  $\nu$  and has a negative peak between two positive peaks. The shape of  $V_3$  is symmetric in the case of gaussian distribution. However, the  $V_3$  of brightness temperature has obvious asymmetry. As universe ionize, the negative peak shifts from high  $\delta T_b$  side to low  $\delta T_b$  side and finally vanishes. The  $V_3$  has positive value at lower  $\delta T_b$  in the early stage of reionization, on the other hand, as we mention before, the positive peak at lower  $\delta T_b$  vanishes in the late stage of reionization. This feature suggests that low density regions and unresolved ionized regions exist at  $z = 8.58$  and  $9.95$ . As bubbles expand, bubbles are merged and are overlapped each other. These overlapped bubbles has many handles made of neutral islands and therefore their  $V_3$  becomes negative.

The feature of MFs for  $\delta T_b$  which explained above is reproduced by using SB-model. In Fig. 6, we show the variation of MFs according to change of  $R_b$ . In order to adjust the  $V_0$  of SB-model similar to the  $V_0$  of our fiducial model (Fig. 5), we set various  $R_b$  and  $\delta_{\text{th}}^{\text{SB}} = 4\sigma_m$ . The basic behavior of evolution of MFs for SB-model is similar to one for our default model as below; the  $V_0$  decrease at  $\delta T_b > 0$  ( $R_b = 17\text{Mpc}$ ), the peak of  $V_1$  shifts from high  $\delta T_b$  side to low  $\delta T_b$  side, the peak of  $V_2$  shifts from high  $\delta T_b$  side to low  $\delta T_b$  side, and finally the  $V_2$  becomes positive at  $\delta T_b > 0$ , the peak of  $V_3$  at high  $\delta T_b$  shifts from high  $\delta T_b$  side to low  $\delta T_b$  side, negative peak at center of  $\delta T_b$  spreads and

positive peak at low  $\delta T_b$  vanishes. These trends relate to evolution of bubble size. SB-model does not reproduce our default model completely. For example, the  $V_3$  of SB-model with  $R_b = 10\text{Mpc}$  has clear negative peak but the  $V_3$  of our fiducial model does not. This difference of shape is caused from ionized bubble property such as size and shape.

### 4.3 Bubble property

The distribution of ionized bubbles and topological structure of the brightness temperature are sensitive to the  $T_{\text{vir}}^{\text{min}}$ . In Fig. 7, we show the  $\delta T_b$  maps with different parameters  $T_{\text{vir}}^{\text{min}} = 5 \times 10^3 [K]$  and  $T_{\text{vir}}^{\text{min}} = 4 \times 10^4 [K]$ . As we can see, the map of  $\delta T_b$  with low  $T_{\text{vir}}^{\text{min}}$  has many ionized and unresolved bubbles. For  $T_{\text{vir}}^{\text{min}} = 4 \times 10^4 [K]$ , on the other hand, ionized bubbles are large and connected. Because higher dense regions do not become ionizing source for the model with high  $T_{\text{vir}}^{\text{min}}$ , the high dense regions remain neutral and high  $\delta T_b$ . In contrast, for the model of low  $T_{\text{vir}}^{\text{min}}$ , many small ionized bubbles exist and almost all higher dense regions are ionized. In Fig. 8, we compare the MFs of  $\delta T_b$  with the one for various  $T_{\text{vir}}^{\text{min}}$  and  $\zeta_{\text{ion}}$  under the condition that the neutral fraction and redshift ( $x_{\text{HI}}, z = 0.51, 8.58$ ) are fixed. Although neutral fraction is fixed, the decrease in the  $V_0$  at  $\delta T_b = 0\text{mK}$  is not same for models with various parameters. The decreases does not correspond to neutral fraction because of smoothing (as we discuss §4.2). Therefore, the reason is expected that the effect of smoothing depends on ionized bubble property such as size and distribution. As  $T_{\text{vir}}^{\text{min}}$  becomes small, the positive peak of  $V_3$  at lower value representing the abundance of isolated bubbles shifts from left to right

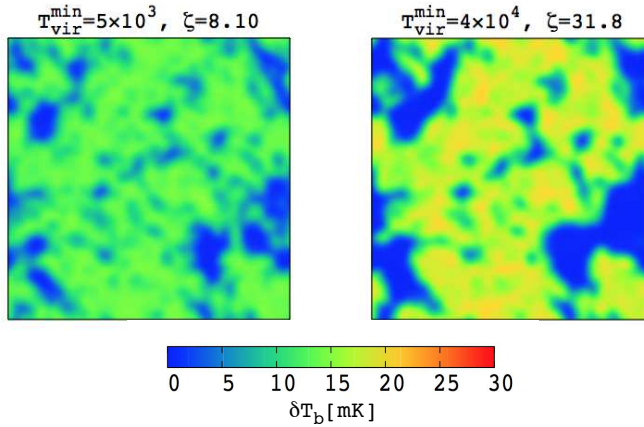


**Figure 7.** Maps of the brightness temperature with various parameters.

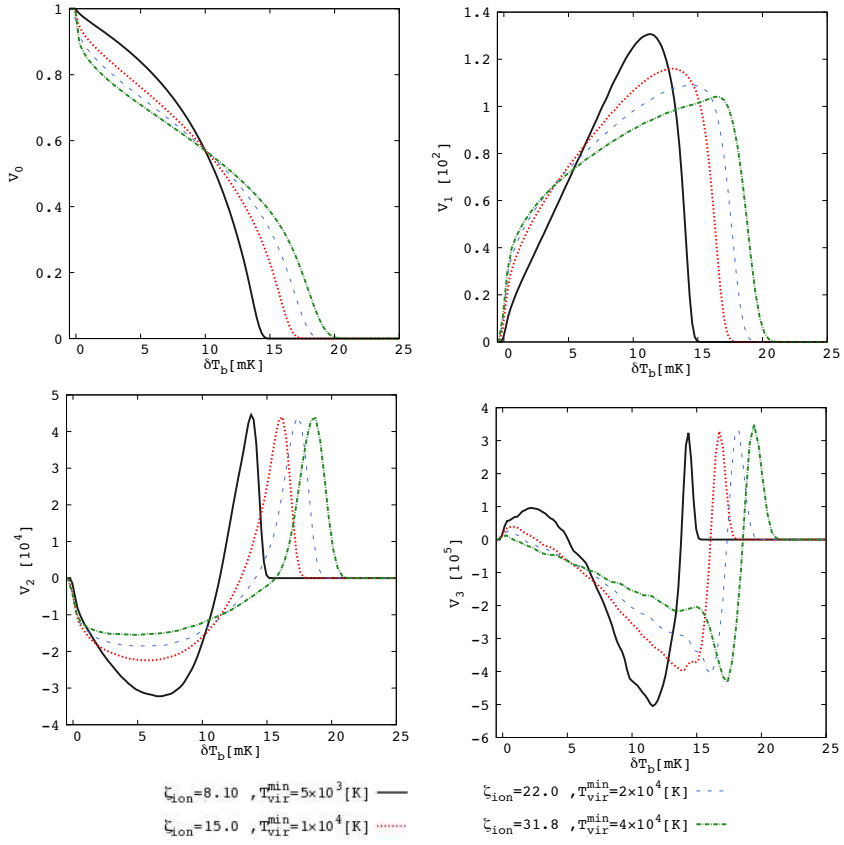


**Figure 8.** MFs with various parameters. All models has same neutral fraction  $x_{HI} \approx 0.511$ . We ignore the spin temperature fluctuation.

and its amplitude becomes large. Because the model with small  $T_{vir}^{\min}$  has many small ionized bubbles smoothed with 5Mpc, many unresolved and isolated bubbles arise between  $\delta T_b \sim 0 - 5$ [mK]. As  $T_{vir}^{\min}$  becomes large, the MFs have non-zero value at high  $\delta T_b$ .

In Fig. 9, we compare the MFs of SB-model with one of various  $\delta_{th}^{\text{SB}}$ , various  $R_b$  with same neutral fraction. The relation between  $\delta_{th}^{\text{SB}}$  and  $R_b$  corresponds to the relation between  $T_{vir}^{\min}$  and  $\zeta_{\text{ion}}$ . In this comparison, the trend of difference for parameter variation toward high threshold is similar to trend toward high  $T_{vir}^{\min}$ . Therefore, the dependence on difference

of bubble distribution is a common characteristic regardless of bubble shape. However, the detailed shape of MFs in Fig. 9 does not correspond to the shape of the MFs in Fig. 8. This fact indicate that the MFs express quantitatively the difference of bubble shape and distribution.

## 5 SUMMARY AND DISCUSSION

In this work, we investigated the topological information of the 21cm-line brightness temperature field during the EoR

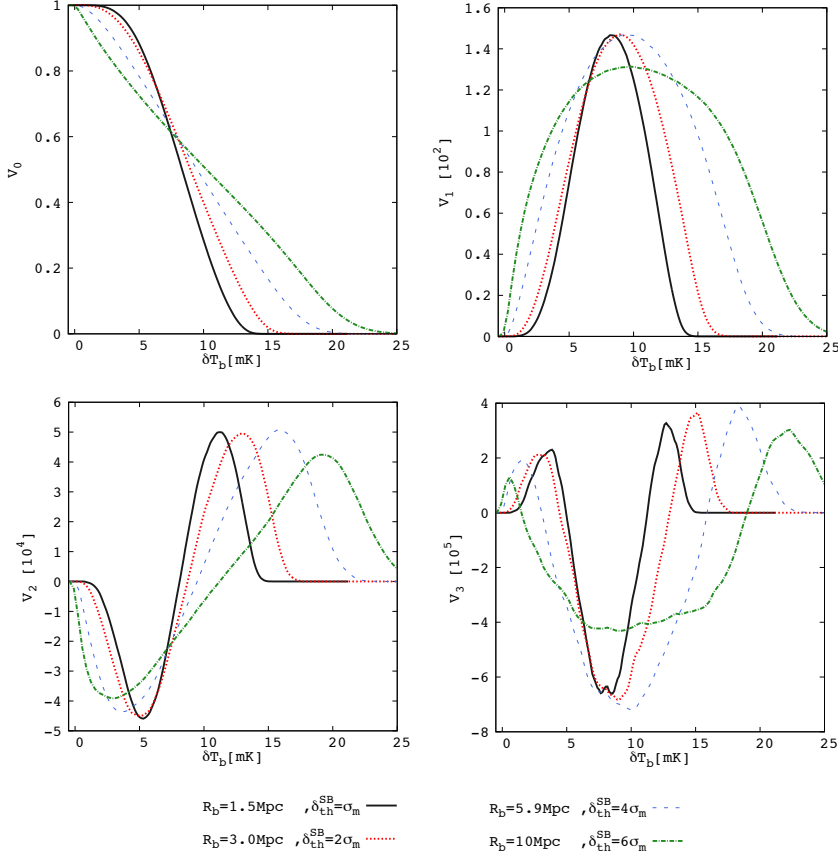


**Figure 9.** MFs for SB-model with various parameters. All models has almost same neutral fraction  $x_{HI} \approx 0.53$ .

by using the Minkowski functionals. We attempted to obtain physical interpretation by comparison with some models. Firstly, we compared the MFs of our “fid” model with the component maps and found that the main component of the EoR structure is the neutral fraction at the late stage of reionization and the spin temperature at the early stage of reionization. Noticeably, the spin temperature can contribute to the structure of  $\delta T_b$  even though the average spin temperature is ten times higher than  $T_\gamma$ . Secondly, we evaluated the MFs evolution at various redshift. The complicated evolution of the MFs as functions of redshift and neutral fraction is understood as the expansion of bubble size. Thirdly, we compared our fiducial model with models with a different value of  $T_{\text{vir}}^{\text{min}}$  and a toy model with spherical ionized bubbles. We found that the minimum virial temperature changes the topology of the IGM and the MFs can distinguish the variation. Therefore, the MFs could be useful for constraining the parameter which relates to the topology of ionized bubbles. Although the trend of parameter dependence is common, “fid” and SB-model do not have precisely the same shape of the MFs. Therefore, the MFs are expected to contain quantitatively both the size and shape of ionized bubbles.

This kind of analysis will be viable when the imaging of 21cm signal becomes possible with a high angular resolution. However, there are many obstacles for imaging such as thermal noise, instrumental contamination and galactic and extragalactic foregrounds. We will estimate constraints

on the EoR model parameters with the MFs including these observational difficulty in the future work.

## ACKNOWLEDGEMENT

This work is supported by Grant-in-Aid from the Ministry of Education, Culture, Sports, Science and Technology (MEXT) of Japan, No. 25-3015 (HS). KT is supported by Grand-in-Aid from the Ministry of Education, Culture, Sports, and Science and Technology (MEXT) of Japan, No. 24340048, No. 26610048 and No. 15H05896. TM acknowledges support from MEXT KAKENHI Grand Number 15K05074 (2015) and 15H05890 (2015).

## REFERENCES

- Beardsley, A. P., Hazelton, B. J., Morales, M. F., et al. 2013, MNRAS, 429, L5
- Carilli, C. 2015, Advancing Astrophysics with the Square Kilometre Array (AASKA14), 171
- Cooray, A., Li, C., & Melchiorri, A. 2008, Phys. Rev. D, 77, 103506
- Dillon, J. S., Neben, A. R., Hewitt, J. N., et al. 2015, Phys. Rev. D, 91, 123011
- Einasto, M., Saar, E., Liivamägi, L. J., et al. 2007, A&A, 476, 697
- Fan, X., Strauss, M. A., Becker, R. H., et al. 2006, AJ, 132, 117
- Furlanetto, S. R., Zaldarriaga, M., & Hernquist, L. 2004, ApJ, 613, 1

Furlanetto, S. R., Oh, S. P., & Briggs, F. H. 2006, *Phys. Rep.*, 433, 181

Friedrich, M. M., Mellema, G., Alvarez, M. A., Shapiro, P. R., & Iliev, I. T. 2011, *MNRAS*, 413, 1353

Gott, J. R., III, Dickinson, M., & Melott, A. L. 1986, *ApJ*, 306, 341

Gleser, L., Nusser, A., Ciardi, B., & Desjacques, V. 2006, *MNRAS*, 370, 1329

Greig, B., & Mesinger, A. 2015, *MNRAS*, 449, 4246

Lee, K.-G., Cen, R., Gott, J. R., III, & Trac, H. 2008, *ApJ*, 675, 8

Lonsdale, C. J., Cappallo, R. J., Morales, M. F., et al. 2009, *IEEE Proceedings*, 97, 1497

Haiman, Z., Abel, T., & Rees, M. J. 2000, *ApJ*, 534, 11

Hasegawa, K., & Semelin, B. 2013, *MNRAS*, 428, 154

Hong, S. E., Ahn, K., Park, C., et al. 2014, *Journal of Korean Astronomical Society*, 47, 49

Jensen, H., Datta, K. K., Mellema, G., et al. 2013, *MNRAS*, 435, 460

Kim, H.-S., Wyithe, J. S. B., Raskutti, S., Lacey, C. G., & Helly, J. C. 2013, *MNRAS*, 428, 2467

Komatsu, E., Dunkley, J., Nolta, M. R., et al. 2009, *ApJS*, 180, 330

Komatsu, E., Smith, K. M., Dunkley, J., et al. 2011, *ApJS*, 192, 18

Matsubara, T. 1994, *ApJ*, 434, L43

McQuinn, M., Lidz, A., Zahn, O., et al. 2007, *MNRAS*, 377, 1043

Mellema, G., Koopmans, L. V. E., Abdalla, F. A., et al. 2013, *Experimental Astronomy*, 36, 235

Mesinger, A., Furlanetto, S., Cen, R. 2011, *MNRAS*, 411, 955

Mesinger, A., Ewall-Wice, A., & Hewitt, J. 2014, *MNRAS*, 439, 3262

Mesinger, A., Ewall-Wice, A., & Hewitt, J. 2014, *MNRAS*, 439, 3262

Parsons, A. R., Backer, D. C., Foster, G. S., et al. 2010, *AJ*, 139, 1468

Parsons, A. R., Liu, A., Aguirre, J. E., et al. 2014, *ApJ*, 788, 106

Pober, J. C., Liu, A., Dillon, J. S., et al. 2014, *ApJ*, 782, 66

Pritchard, J. R., & Furlanetto, S. R. 2006, *MNRAS*, 367, 1057

Pritchard, J. R., & Furlanetto, S. R. 2007, *MNRAS*, 376, 1680

Schmalzing, J., & Buchert, T. 1997, *ApJ*, 482, L1

Shimabukuro, H., Yoshiura, S., Takahashi, K., Yokoyama, S., & Ichiki, K. 2014, arXiv:1412.3332

Shimabukuro, H., Yoshiura, S., Takahashi, K., Yokoyama, S., & Ichiki, K. 2015, arXiv:1507.01335

Sobacchi, E., & Mesinger, A. 2014, *MNRAS*, 440, 1662

Tingay, S. J., Goeke, R., Bowman, J. D., et al. 2013, *Publ. Astron. Soc. Australia*, 30, e007

van Haarlem, M. P., Wise, M. W., Gunst, A. W., et al. 2013, *A&A*, 556, A2

Wang, Y., Park, C., Xu, Y., Chen, X., & Kim, J. 2015, *ApJ*, 814, 6

Zahn, O., Lidz, A., McQuinn, M., et al. 2007, *ApJ*, 654, 12

This paper has been typeset from a *TeX/LaTeX* file prepared by the author.